New Journal of Physics
The open access journal at the forefront of physics

Deutsche Physikalische Gesellschaft DPG
IOP Institute of Physics

Published in partnership with: Deutsche Physikalische Gesellschaft and the Institute of Physics

OPEN ACCESS

RECEIVED
9 February 2017

REVISED
27 April 2017

ACCEPTED FOR PUBLICATION
12 May 2017

PUBLISHED
10 July 2017

PAPER

Distribution functions of magnetic nanoparticles determined by a numerical inversion method

P Bender[1], C Balceris[2], F Ludwig[2], O Posth[3], L K Bogart[4], W Szczerba[5,6], A Castro[7], L Nilsson[7,8], R Costo[9], H Gavilán[9], D González-Alonso[10], I de Pedro[10], L Fernández Barquín[10] and C Johansson[11]

[1] Departamento CITIMAC, Faculty of Science, University of Cantabria, E-39005 Santander, Spain
[2] Institut für Elektrische Messtechnik und Grundlagen der Elektrotechnik, TU Braunschweig, D-38106 Braunschweig, Germany
[3] Physikalisch-Technische Bundesanstalt, Abbestr. 2-12, D-10587 Berlin, Germany
[4] UCL Healthcare Biomagnetics Laboratory, University College London, 21 Albemarle Street, London W1S 4BS, United Kingdom
[5] Bundesanstalt für Materialforschung und -prüfung, D-12205 Berlin, Germany
[6] AGH University of Science and Technology, Academic Centre for Materials and Nanotechnology, Al. A. Mickiewicza 30, PL-30059 Krakow, Poland
[7] SOLVE Research and Consultancy AB, SE-223 63 Lund, Sweden
[8] Lund Centre for Field-Flow Fractionation, Department of Food Technology, Engineering and Nutrition, Lund University, SE-223 63 Lund, Sweden
[9] Instituto de Ciencia de Materiales de Madrid, ICMM/CSIC, E-28049 Madrid, Spain
[10] Departmento CITIMAC, Faculty of Science, University of Cantabria, E-39005 Santander, Spain
[11] RISE Acreo AB, SE-40014 Göteborg, Sweden

E-mail: benderpf@unican.es

Keywords: magnetic nanoparticles, numerical inversion, SAXS, magnetization measurements, AC susceptibility, distribution functions

Abstract

In the present study, we applied a regularized inversion method to extract the particle size, magnetic moment and relaxation-time distribution of magnetic nanoparticles from small-angle x-ray scattering (SAXS), DC magnetization (DCM) and AC susceptibility (ACS) measurements. For the measurements the particles were colloidally dispersed in water. At first approximation the particles could be assumed to be spherically shaped and homogeneously magnetized single-domain particles. As model functions for the inversion, we used the particle form factor of a sphere (SAXS), the Langevin function (DCM) and the Debye model (ACS). The extracted distributions exhibited features/peaks that could be distinctly attributed to the individually dispersed and non-interacting nanoparticles. Further analysis of these peaks enabled, in combination with a prior characterization of the particle ensemble by electron microscopy and dynamic light scattering, a detailed structural and magnetic characterization of the particles. Additionally, all three extracted distributions featured peaks, which indicated deviations of the scattering (SAXS), magnetization (DCM) or relaxation (ACS) behavior from the one expected for individually dispersed, homogeneously magnetized nanoparticles. These deviations could be mainly attributed to partial agglomeration (SAXS, DCM, ACS), uncorrelated surface spins (DCM) and/or intra-well relaxation processes (ACS). The main advantage of the numerical inversion method is that no *ad hoc* assumptions regarding the line shape of the extracted distribution functions are required, which enabled the detection of these contributions. We highlighted this by comparing the results with the results obtained by standard model fits, where the functional form of the distributions was *a priori* assumed to be log-normal shaped.

1. Introduction

As evident from recent review articles [1–4], biomedical application of magnetic iron oxide nanoparticles (IONPs) is presently an intensely investigated, multi-disciplinary field of research. However, to this day there exists no standardized way of characterizing IONPs. In this sense, regulatory work is necessary prior to clinical application to guarantee a safe and effective implementation of IONPs [5, 6]. To disclose unambiguously the

interrelations between structural and magnetic properties of ensembles of IONPs usually a combination of several techniques is applied, such as transmission electron microscopy (TEM), dynamic light scattering (DLS), small-angle x-ray scattering (SAXS), DC magnetization (DCM) and AC susceptibility (ACS) measurements. The standardization process then should include a precise control of the measurement procedures itself as well as of the data analysis.

The theoretical framework defining the interrelations between particle structure and magnetic properties is well established in the ideal case of homogeneously magnetized, single-domain and non-interacting particles [7–9]. The same applies to the relaxation dynamics of colloidally dispersed magnetic nanoparticles. These relations are commonly used to extract for example the intrinsic core or hydrodynamic size distributions from DCM [10–12] or ACS measurements [13, 14]. As model functions for DCM and ACS measurements, the Langevin function [15] (DCM) and Debye model [16] (ACS) are used, respectively. The classical approach to extract the characteristic distributions is to fit the experimental data with the respective model function under assumptions regarding the line shape. Usually a log-normal shape is *a priori* assumed for the intrinsic distributions [10–14]. But several factors can result in deviations of the macroscopically determined, apparent distribution functions from the intrinsic ones. In particular dipolar interactions can lead to particle agglomeration [17–20], which can significantly modify the macroscopically detected magnetization behavior of the particle ensemble. To infer the intrinsic moment or relaxation time distribution from data fits, several mean field approaches exist to analytically model the influence of dipolar interactions on isothermal [21–23] or dynamic magnetization measurements [24, 25], respectively.

However, an alternative approach to analytical model fits can be found in the literature. In [26–29] for example, the discrete, apparent moment distributions of IONP ensembles were extracted from $M(H)$ data numerically, using simply the Langevin equation as a model function. In these cases no *a priori* assumptions regarding the line shape of the extracted distribution have to be made and data analysis is ultimately performed by interpreting the obtained apparent distributions. Similar numerical approaches are also commonly used to infer the hydrodynamic size distribution of nanoparticles from DLS measurements [30, 31] or to analyze the small-angle scattering data of nanoparticle ensembles [32–36].

In the current work we use the same numerical approach as applied in [36] for the analysis of magnetic multi-core nanoparticles to systematically evaluate SAXS, DCM and ACS data of a dilute, colloidal dispersion of single-domain IONPs. Initially, we extracted the discrete particle size distribution from the SAXS data, the moment distribution from the DCM data and the relaxation time distribution from the ACS data. Afterwards, we further analyzed the distributions to disclose the relations between the structural and the magnetic properties of the nanoparticles. This approach, in combination with classical TEM and DLS analysis, as well as magnetization measurements of the immobilized particles, enabled us to perform a very detailed characterization of the IONP ensemble. Additionally, we highlight the influence of particle agglomeration and/or uncorrelated surface spins on the measurement signals by comparing the extracted distributions to the results of standard model fits, where a log-normal shape of the distributions was *a priori* assumed.

2. Experimental procedure

The synthesis of the IONPs was carried out by thermal decomposition of an iron oleate complex mixed with oleic acid in 1-octadecene [37]. In a round-bottomed flask equipped with a mechanical stirrer and a reflux condenser under a nitrogen flow, the iron(III) oleate (4.5 g, 5 mmol, 7% iron) was mixed with oleic acid (0.7 g) in 1-octadecene (50 ml). The mixture was stirred and heated up until reflux (320 °C) at 3 °C min^{-1} with a heating mantle. Stirring and nitrogen flow were stopped once the temperature reached 100 °C. The resulting suspension was washed with ethanol, centrifuged at 3944 g and redispersed by agitation (ten times). The precipitated particles were finally dried under a nitrogen flow, redispersed in toluene and transferred to water by ligand exchange with dimercaptosuccinic acid (DMSA) [38]. The pH value of the final water-based colloidal dispersion of the nanoparticles was adjusted to 7. This colloidal dispersion was directly measured by SAXS, DCM and ACS without any sample modification, although for ACS the sample was diluted ten-fold with distilled water.

To determine the amount of iron within the colloidal dispersion and hence estimate the particle concentration, inductively coupled plasma optical emission spectrometry (ICP-OES) was carried with an apparatus from Perkin Elmer, model OPTIME 2100DV. The wavelengths used for iron determination were 238.204 and 239.562 nm. For an appropriate determination it is necessary to digest the nanoparticle dispersion prior to analysis. An aliquot of sample (50 μl) was mixed with 2 ml of HCl until complete digestion was obtained.

The main structural properties of the sample were determined by TEM, DLS and finally SAXS.

To obtain the core-size distribution, images of the particles were taken using a 200 keV JEOL-2000 FXII TEM and the largest dimension of 500 particles was measured.

The hydrodynamic size of the particles dispersed in water was measured with a ZETASIZER NANO-ZS device (Malvern Instruments) using the DLS mode. The measurements of the 100-fold diluted dispersion were done at 25 °C with an equilibration time of 60 s. A measurement consisted of 24 runs, with acquisition times of 10 s. The hydrodynamic diameter, or z-average, as well as the polydispersity index *PDI*, was derived from the cumulant analysis, wherein a single particle size was assumed and a single exponential fit was applied to the autocorrelation function.

The SAXS measurement of the colloidal dispersion of IONPs was carried out on a Kratky system with slit focus, SAXSess by Anton Paar, Graz, Austria. The measurement was performed as an absolute intensity measurement by also measuring the scattering curves of the empty capillary and water. These were subtracted from the measured scattering curve of the sample during the data reduction procedure using the implemented SAXSquant software. The resultant curve was deconvoluted with the beam profile curve to correct for the slit focus smearing.

The magnetic properties of the particles were determined by measuring the isothermal magnetization curve of both the immobilized as well as colloidally dispersed particles.

To immobilize the particles and hence suppress a rotation of the particles in the field direction, a droplet of 5 μl of the colloidal dispersion was put on cotton wool. The isothermal magnetization measurement was recorded with a Quantum design SQUID VSM 7T with Quick Switch and Evercool at 300 K in a field range of $\mu_0 H = \pm 7$ T.

The isothermal DCM measurement of the colloidal dispersion of IONPs was performed at 300 K in a magnetic property measurement system (MPMS XL, Quantum Design, USA). The magnetic field was varied in the field range $\mu_0 H = 0 \pm 4.9$ T and the size of the consecutive field step was changed logarithmically to ensure a sufficient number of measurements at low fields. The time between each field step was about 3 min, providing quasi-static measurement conditions. A volume of 30 μl of the suspension was measured a total of five times with the same measurement conditions and the data points were averaged. From the data the diamagnetic contributions of the empty sample holder and the water were subtracted. The corrected magnetic moment in A m^2 was normalized to the mass of iron determined by ICP-OES to obtain the magnetization in A m^2 kg$_{\mathrm{Fe}}^{-1}$.

To investigate the relaxation dynamics of the particles dispersed in water the colloidal dispersion was measured using ACS. The measurement was performed at 300 K utilizing two custom-built susceptometers [13]. The frequency was swept from 10 Hz to 10 kHz and from 200 Hz to 1 MHz in logarithmical steps. The amplitudes of the excitation field amounted to 567 μT and 90 μT, respectively, to ensure that the magnetization response was in the linear regime. To suppress hydrodynamic interactions between the particles, the dispersion was diluted ten-fold. A total volume of 150 μL of the resulting colloid was measured. To convert the measured signal to volume susceptibility $\tilde{\chi}(\omega)$, both systems were calibrated with Dy_2O_3 powder samples with known susceptibility. Since the measurement was performed only once, for each data point a noise of $0.01\chi'_{\mathrm{max}}$ was artificially added.

3. Theoretical framework

In this section we present the theoretical background regarding the magnetic properties of colloidally dispersed IONPs. On this basis, the approaches to analyze the experimental data of the SAXS, DCM and ACS measurements of the colloidal dispersion are introduced.

3.1. Background

Within this work we assume that the IONPs are spherically shaped with a core diameter d_c (figure 1) and are single-domain particles. Experimental studies and simulations [39–44] indicate that the atomic spins at the surface of magnetic nanoparticles are usually disordered due to lack of coordination, vacancies and/or surface anisotropy. This can be depicted by a core–shell structure of the particle with $d_m < d_c$, where d_m is the diameter of the homogeneously magnetized core (single-domain, figure 1). Therefore, in the following we will differentiate between the total core volume $V_c = (1/6)\pi d_c^3$ and the magnetic core volume $V_m = (1/6)\pi d_m^3$, in which the atomic spins are parallel aligned. In this case the total particle moment $\vec{\mu}$ can be represented by a macrospin with magnitude $|\vec{\mu}| = M_S V_m$, where M_S is the material specific saturation magnetization. The bulk values for the two iron oxides magnetite Fe_3O_4 and maghemite $\gamma - Fe_2O_3$ at $T = 300$ K are listed in table 1, as well as other intrinsic properties relevant for the current study [7, 9].

In the case of isothermal DCM measurements it can be estimated that for particles with $KV_m \leqslant 25 k_B T$ [7, 9] thermal activation results in a fluctuation of the moment (superparamagnetism). Here K is the effective anisotropy constant and k_B the Boltzmann constant. Thus, theoretically, magnetite particles with diameters

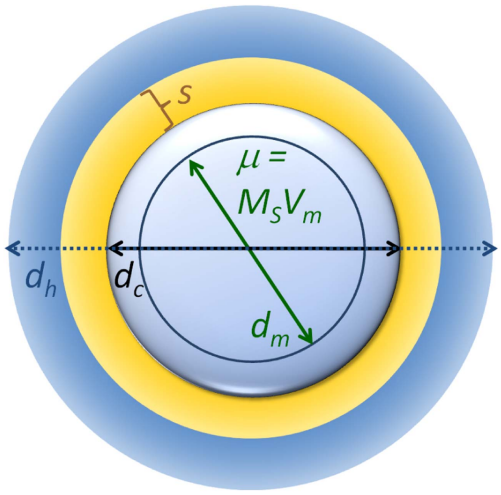

Figure 1. Schematic illustration of the characteristic sizes of a single-core particle with diameter d_c dispersed in water. The diameter d_m represents the size of the homogeneously magnetized core (single-domain; parallel aligned atomic spins), s is the thickness of the surrounding polymer layer and d_h the hydrodynamic diameter.

Table 1. Intrinsic properties of Fe_3O_4 and $\gamma - Fe_2O_3$ at $T = 300$ K [7, 9]. Here ρ is the volumetric mass density, w_{Fe} the weight percentage of iron, M_S the saturation magnetization, K_1 the first order magnetocrystalline anisotropy constant and ρ_s the scattering length density. The scattering length density of water is $\rho_s^{H_2O} = 9.5 \times 10^{-4}$ nm^{-2}.

	ρ kg m^{-1}	w_{Fe} wt%	M_S MA m^{-1}	M_S A m^2 kg$_{Fe}^{-1}$	$\lvert K_1 \rvert$ kJ m^{-3}	ρ_s nm^{-2}
Fe_3O_4	5195	0.72	0.48	128.3	13	40.6×10^{-4}
$\gamma - Fe_2O_3$	4860	0.70	0.40	117.6	5	38.1×10^{-4}

$d_m < d_{SP} = 25$ nm and maghemite particles with $d_m < d_{SP} = 34$ nm behave intrinsically superparamagnetically. For these calculations it was assumed that the effective anisotropy constants K for magnetite and maghemite are the magnitude of their first order magnetocrystalline anisotropy constants $|K_1|$ (table 1). Consequently, an alignment of the moments of particles with $d_m < d_{SP}$ in the direction of an externally applied static field can occur by the Néel mechanism [45]. The moments of thermally blocked particles with $d_m > d_{SP}$ dispersed in a viscous matrix on the other hand, can only align in the field direction by a rotation of the entire particle, the so-called Brownian rotation. In the case of DCM measurements, the magnetization behavior of one macrospin dispersed in a purely viscous matrix is independent of the alignment process and can be described by the Langevin function [15]:

$$M(H)/M_S = L(H, \mu) = \coth\frac{\mu\mu_0 H}{k_B T} - \frac{k_B T}{\mu\mu_0 H}. \quad (1)$$

Here $\mu_0 = 4\pi \times 10^{-7}$ V s A^{-1} m^{-1} is the vacuum permeability. In the case of time-modulated fields, however, quantitatively the response critically depends on the relaxation mechanism.

In an ACS measurement, an alternating magnetic field $\tilde{H}(\omega) = H_0 \exp(i\omega t)$ with amplitude H_0 and angular frequency ω is applied. The response is a periodic change in the magnetization $\tilde{M}$, following the driving field with a frequency dependent time lag due to friction ($\tilde{M}(\omega) = \tilde{\chi}(\omega) \cdot \tilde{H}(\omega)$). For small amplitudes (i.e. $\xi = \frac{\mu\mu_0 H_0}{k_B T} \ll 1$) the complex susceptibility $\tilde{\chi}(\omega)$ can be described by the Debye relaxation $\tilde{\chi}_D(\omega) = \chi'_D(\omega) - i\chi''_D(\omega)$ with [16]

$$\tilde{\chi}_D(\omega) = \frac{\chi_0}{1 + i\omega\tau}, \text{ with: } \chi_0 = \frac{\mu\mu_0 M_S}{3k_B T}. \quad (2)$$

In equation (2) the time constant τ is the effective relaxation time given by $\tau = \tau_n \cdot \tau_b/(\tau_n + \tau_b)$, with τ_n being the Néel relaxation time

$$\tau_n = \tau_0 \exp\left(\frac{K\pi d_m^3}{6k_B T}\right) \quad (3)$$

and τ_b being the Brownian relaxation time:

$$\tau_b = \frac{\pi \eta d_h^3}{2 k_B T}. \quad (4)$$

The time constant τ_0 in equation (3) is generally taken as 10^{-9} s [13]. In equation (4), η is the viscosity of the surrounding medium and d_h the hydrodynamic diameter of the particle (figure 1). The hydrodynamic diameter is usually larger than the core diameter d_c due to a surfactant shell and additional friction contributions, such as surface charges [46]. The effective relaxation time $\tau = \tau_n \cdot \tau_b/(\tau_n + \tau_b)$ is dominated by the faster process and as a result the measurement signal of the ACS experiments are sensitive to the respective relaxation process [47].

As depicted above, the quasi-static and dynamic magnetic properties critically depend on the structural properties of the particles. Within this work we determined the core size d_c of the particles by TEM and SAXS, the hydrodynamic size d_h by DLS, the magnetic moment μ and magnetic core size d_m by DCM, and the relaxation time τ by ACS. The main objective was to correlate the various parameters. When characterizing nanoparticle ensembles it has to be considered that the core and hydrodynamic sizes usually have a distribution width, and thus also magnetic moments as well as relaxation times [48]. In the following we explain how the various distributions were determined in this study.

3.2. Data analysis

With TEM the core-size distribution was directly obtained by measuring $N = 500$ particles and the DLS setup provided the detected hydrodynamic size distribution. Both techniques were used for the pre-characterization of the sample.

In the case of SAXS, DCM and ACS the relevant distribution $p(z)$ of parameter z had to be extracted from the data $D(x)$. For SAXS $D(x)$ is the scattering intensity $I(q)$, with q being the scattering vector and $p(z) = p(d_c)$. In the case of DCM $D(x) = M(H)$ and $p(z) = p(\mu)$ or $p(z) = p(d_m)$, whereas for ACS $D(x) = \chi'(\omega)$ and/or $\chi''(\omega)$ and $p(z) = p(\tau)$. The distribution $p(z)$ describes the continuous probability density function of the paramater z and it can be written

$$D(x) = c \int_0^\infty p(z) f(x, z)\, dz. \quad (5)$$

Here c is a characteristic prefactor and $f(x, z)$ the corresponding model function.

To determine $p(z)$ from the experimental data we applied two approaches in this study. (1) By a standard least square fit of the data under the assumption of a log-normal distribution $p(z)$. (2) By numerical inversion without *a priori* assumptions regarding the line shape.

3.2.1. Log-normal fit

With respect to magnetic nanoparticle ensembles it is often assumed that the particle size is logarithmically distributed, resulting in log-normal distributions of the magnetic moments [10–12] and relaxation times [13]. The probability density of a log-normally distributed variable z is

$$p(z) = \frac{1}{\sqrt{2\pi}\sigma z} \exp\left(\frac{-\ln(z/\bar{z})^2}{2\sigma^2}\right), \quad (6)$$

where σ is the standard deviation of the log of the distribution, $\bar{z}$ the median and $\langle z \rangle = \bar{z} \cdot \exp\left(\frac{\sigma^2}{2}\right)$ the mean value. For comparison purposes between the different distributions, it is important to consider that they vary with respect to their weighting, depending on the nature of the applied technique. In this work it has to be differentiated between number-weighted distributions p_N and volume-weighted distributions p_V [49]. The characteristic values of these distributions—such as broadness, median and arithmetic mean—are subscripted in the following always with either N or V to indicate whether they correspond to the number or volume-weighted distribution, respectively. For number and volume-weighted log-normal distributions the standard deviations are in theory identical ($\sigma_V = \sigma_N = \sigma$) but the medians $\bar{z}_V$ and $\bar{z}_N$ are shifted. In the case of homogeneous spheres, e.g. $\bar{z}_V = \bar{z}_N \cdot \exp(3\sigma^2)$ [49].

In this work we determined the number-weighted core-size distribution $p_N(d_c)$ by fitting the SAXS intensity $D(x) = I(q)$ with [50]

$$I(q) = \phi_p \Delta\rho_s^2 \frac{\int_0^\infty p_N(d_c) F(q, d_c)\, dd_c}{\int_0^\infty p_N(d_c) V_c(d_c)\, dd_c} + bkg. \quad (7)$$

Here ϕ_p is the volume fraction of particles, $\Delta\rho_s$ the scattering length density contrast between the particles and the surrounding medium (table 1) and *bkg* the background level due to incoherent scattering. As a model function we used the form factor $F(q, d_c)$ of a homogeneous sphere [50]:

$$F(q,\, d_c) = \left(V_c \frac{3\left[\sin\left(\frac{qd_c}{2}\right) - \frac{qd_c}{2}\cos\left(\frac{qd_c}{2}\right)\right]}{\left(\frac{qd_c}{2}\right)^3} \right)^2. \tag{8}$$

From the magnetization data $M(H)$ the volume-weighted moment distribution $p_V(\mu)$ can be extracted by fitting with [11]

$$M(H) = M_S \int_0^\infty p_V(\mu) L(H,\, \mu) \mathrm{d}\mu. \tag{9}$$

To determine the number-weighted magnetic core diameter distribution $p_N(d_m)$ we modeled the data in this work with [11]:

$$M(H) = M_S \frac{\int_0^\infty p_N(d_m) d_m^3 L(H,\, \mu(d_m)) \mathrm{d}d_m}{\int_0^\infty p_N(d_m) d_m^3 \mathrm{d}d_m}. \tag{10}$$

From the ACS measurements the relaxation time distribution can be extracted by fitting the ACS spectra with

$$\tilde{\chi}(\omega) = \chi_0^* \int_0^\infty p(\tau) \frac{1}{1 + \mathrm{i}\omega\tau} \mathrm{d}\tau. \tag{11}$$

In this case the prefactor χ_0^* as well as the weighting of the relaxation time distribution $p(\tau)$ critically depends on the correlation between the particle moments μ and τ [14]. For the simple case that they are not correlated $\chi_0^* = n\mu_0 M_S^2 \langle V_{m,N}^2 \rangle / (3k_B T)$, with n being the particle concentration, $\langle V_{m,N} \rangle$ is the number-weighted mean magnetic core volume, and $p(\tau)$ is number-weighted. Normally, however, a correlation between μ and τ has to be considered, as discussed for example in [14, 51, 52].

3.2.2. Numerical inversion

At each of the $i = M$ data points $D(x_i)$ the integral equation (5) can be discretized:

$$D(x_i) = c \sum_{j=1}^{N} p(z_j) f(x_i,\, z_j) \Delta z_j. \tag{12}$$

Here $j = N$ is the number of bins of the reconstructed histogram $p(z)$ with width Δz, where $p(z)$ represents the probability density function of the variable z so that $\int_0^\infty p(z) = 1$. To extract the N-dimensional vector $P(z)$ with $P(z_j) = c \cdot p(z_j)\Delta z_j$ the functional

$$\frac{1}{2\sigma^2} \|\mathbf{A}P(z) - D(x)\|^2 \tag{13}$$

has to be minimized, with $\sigma = \sigma(x)$ being the measurement uncertainty or standard deviation at each data point. In equation (13) $\mathbf{A}$ is the $M \times N$ data transfer matrix with $A_{i,j} = f(x_i,\, z_j)$.

For SAXS $f(x_i,\, z_j) = F(q_i,\, d_{c,j})$ (equation (8)) and the number-weighted core-size distribution $p_N(d_c)$ was extracted with (equation (12)):

$$I(q_i) = c_S \sum_{j=1}^{N} p_N(d_{c,j}) F(q_i,\, d_{c,j}) \Delta d_{c,j} + bkg. \tag{14}$$

Comparison with equation (7) shows that $c_S = \phi_p \Delta\rho_s^2 / \langle V_{c,N} \rangle$, with $\langle V_{c,N} \rangle = \sum_{j=1}^{N} p_N(d_{c,j}) V_c(d_{c,j}) \Delta d_c$ being the number-weighted mean particle volume.

For DCM $f(x_i,\, z_j) = L(H_i,\, \mu_j)$ (equation (1)) and from $M(H)$ the volume-weighted moment distribution $p_V(\mu)$ was extracted according to:

$$M(H_i) = c_D \sum_{j=1}^{N} p_V(\mu_j) L(H_i,\, \mu_j) \Delta\mu_j. \tag{15}$$

In this case $c_D = M_S$ (equation (9)).

For ACS $f(x_i,\, z_j) = \tilde{\chi}_D(w_i,\, \tau_j)/\chi_0$ (equation (2)) and from the measurement the relaxation time distribution $p(\tau)$ was determined by simultaneously adjusting the real and imaginary part of the complex volume susceptibility $\tilde{\chi}(\omega)$:

$$\tilde{\chi}(\omega_i) = c_A \sum_{j=1}^{N} p(\tau_j) \frac{1}{1 + i\omega_i\tau_j} \Delta\tau_j. \tag{16}$$

Here $c_A = \chi_0^*$ (equation (11)). As discussed above, the prefactor χ_0^* and the weighting of the relaxation time distribution depends on the correlation between μ and τ. For further details regarding this issue see [14, 51, 52].

Solving of equation (13), however, is an ill-conditioned problem. Therefore, we implemented a non-negative constraint and additionally applied a regularized inversion. To determine the probability for a given

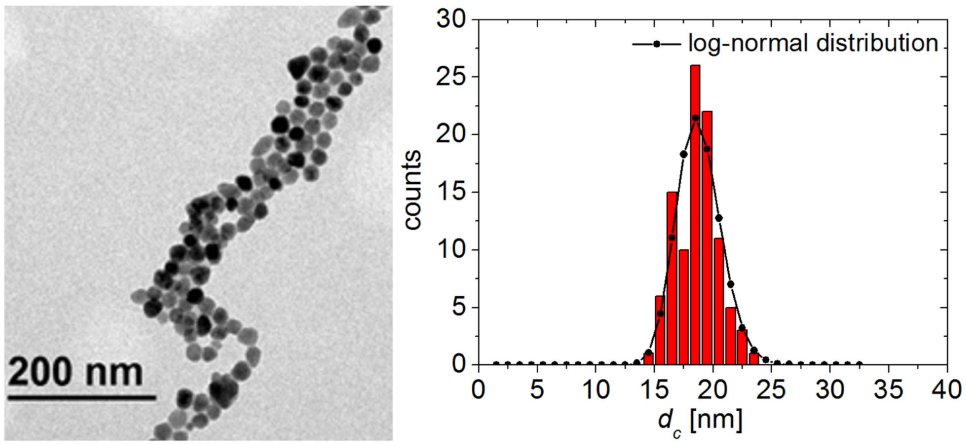

Figure 2. TEM micrograph of the particles and the histogram of the core diameter d_c fitted with a log-normal distribution ($\sigma = 0.10(1)$, $\bar{d}_{c,N} = 18.7(3)$ nm, table 2).

regularization parameter we performed a Bayesian analysis, as introduced in [34, 35]. The computational details can be found in the appendix.

For a detailed analysis and interpretation of the extracted distributions a pre-characterization of the sample was necessary. A structural pre-characterization included the measurement of the iron concentration in the colloidal dispersion by ICP-OES as well as the determination of the core-size distribution $p(d_c)$ by TEM and the hydrodynamic size distribution $p(d_h)$ of the particles in dispersion by DLS. Additionally, we characterized the magnetic properties of the immobilized particles to estimate the number of thermally blocked particles at 300 K.

4. Pre-characterization of the nanoparticles

With ICP-OES the iron concentration of the sample was determined to be $c_{Fe} = 4.23\ mg_{Fe}\ mL^{-1}$. Using the density of magnetite or maghemite (table 1), the volume fraction of particles in the colloidal dispersion could be estimated to be $\phi_p^{Fe_3O_4} = 1.13 \times 10^{-3}$ and to be $\phi_p^{\gamma-Fe_2O_3} = 1.24 \times 10^{-3}$, respectively.

Figure 2 shows a representative TEM image of the IONPs. The histogram (figure 2) represents the number-weighted distribution P_N of the core diameter d_c and was fitted with the probability density $p(z)$ (equation (6)) of a log-normal distribution function scaled by c ($P_N(d_c) = c \cdot p_N(d_c)$). The best fit result was obtained for $\sigma_N = \sigma = 0.10(1)$ and $\bar{d}_{c,N} = 18.7(3)$ nm. The resulting arithmetic mean of the core diameter is then $\langle d_{c,N} \rangle = 18.8(3)$ nm.

With DLS the intensity-weighted hydrodynamic diameter or z-average was determined to be $\langle d_{h,I} \rangle = 52(2)$ nm and the polydispersity index $PDI = 0.53(2)$. The z-average is significantly above $\langle d_{c,N} \rangle = 18.8(1)$ nm, which can be primarily attributed to an increased hydrodynamic volume due to the surfactant layer and surface charges (figure 1). Additionally, it has to be considered that with DLS the determined hydrodynamic size is intensity-weighted and hence the signal is dominated by large particles.

Considering the quite large size of the particles it was important to monitor the stability of the colloidal dispersion. With a core diameter of about 19 nm and assuming a homogeneous magnetization with $M_S = 0.48$ MAm (table 1), the dipolar energy between two neighboring particles with parallel aligned moments can be estimated [22] to be in the range of $10 k_B T$. Thus, dipolar interactions could lead to particle agglomeration and ultimately coagulation. However, the measured z-average and PDI basically did not change over a time span of 15 months, and no sedimentation was observed. In addition, the measured zeta potential remained constant over time and was determined to be about -30 mV. The same applied for the pH value, which remained at 7, and hence we can conclude that the sample remained stable over time across all metrics. We attributed the colloidal stability to the comparatively low volume concentration of nanoparticles, and their surrounding surfactant layer and surface charge.

Later on, the SAXS, DCM and ACS measurements of the colloidally dispersed IONPs are analyzed. In a colloidal dispersion, the static magnetization behavior of thermally blocked and non-blocked (superparamagnetic) particles is identical, provided the particles are individually dispersed in the viscous matrix. Hence, to estimate the amount of thermally blocked particles a physical rotation (Brownian rotation) of the particles has to be suppressed. Additionally, large average distances between the particles have to be assured to avoid dipolar interactions, which can significantly alter the magnetization behavior of such ensembles [53, 54]. For this purpose the particles were immobilized and measured as discussed in section 2.

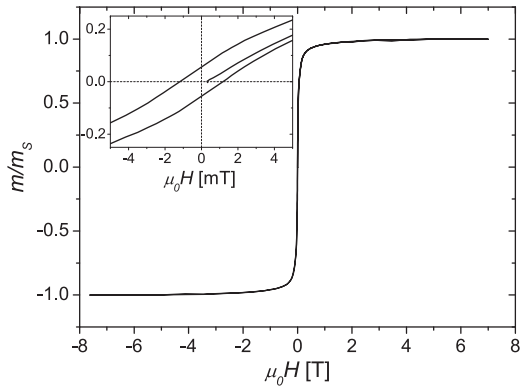

Figure 3. Normalized isothermal magnetization curve $m(H)/m_S$ of the particles deposited on cotton wool. The inset shows the hysteretic behavior with a normalized remanence of $m_r/m_S = 0.06$.

Table 2. Main results of the structural and magnetic pre-characterization. ICP-OES: iron concentration c_{Fe} in the colloidal dispersion and particle concentration ϕ_p in the colloidal dispersion calculated assuming stoichiometry of magnetite or maghemite. TEM: number-weighted log-normal distribution of core size d_c with broadness σ, median value $\bar{d}_{c,N}$ and mean value $\langle d_{c,N}\rangle$. DLS: intensity-weighted hydrodynamic size or z-average $\langle d_{h,I}\rangle$ and polydispersity index *PDI* (in the case of a log-normal distribution, *PDI* and broadness σ are related by: $\sigma = \sqrt{\ln(1 + PDI)}$). DCM: volume fraction of particles behaving superparamagnetically (ϕ_{SP}) and thermally blocked (ϕ_{TB}) at 300 K.

ICP-OES		TEM		DLS		DCM (immobilized)	
c_{Fe}	4.23 mg_{Fe} mL^{-1}	σ	0.10(1)	*PDI*	0.53(2)	ϕ_{SP}	0.88
$\phi_p^{Fe_3O_4}$	1.13×10^{-3}	$\bar{d}_{c,N}$	18.7(3) nm	$\langle d_{h,I}\rangle$	52(2) nm	ϕ_{TB}	0.12
$\phi_p^{\gamma-Fe_2O_3}$	1.24×10^{-3}	$\langle d_{c,N}\rangle$	18.8(3) nm				

Figure 3 shows the magnetic moments $m(H)$ of the immobilized IONPs normalized to the saturation moment m_S of the sample, as a function of the applied field H. The determined coercive field was $\mu_0 H_c = 1.3$ mT and the normalized remanence $m_r/m_S = 0.06$. For an ensemble of particles with uniaxial magnetic anisotropy and with a random orientation distribution of the anisotropy axes (isotropic Stoner–Wohlfarth particle ensemble [55]) the expected normalized remanence would be $m_r/m_S = 0.5$. The detected remanence of the sample of just $m_r/m_S = 0.06$ indicates that, as expected, a significant number of particles behave superparamagnetically at $T = 300$ K. The volume fraction of superparamagnetic particles within the ensemble can be estimated to be $\phi_{SP} \approx 1\text{–}2 \cdot m_r/m_S = 0.88$. This means that a volume fraction of $\phi_{TB} = 0.12$ is thermally blocked at $T = 300$ K.

The main results of the structural and magnetic pre-characterization of the sample are shown in table 2, which are essential for interpreting the results of SAXS, DCM and ACS in the following.

5. Analysis of distribution functions

In this section we present and discuss the particle size, magnetic moment and relaxation time distributions determined from the SAXS, DCM and ACS measurements of the colloidal dispersion. First, we estimated the distributions in each case by fitting the data under the usual assumption of log-normal shape. Afterwards, we determined the discrete, apparent distributions by numerical inversion without *a priori* assumptions regarding the line shape. We analyzed the discrete distributions further to extract the core size (SAXS), magnetic core size (DCM) and hydrodynamic size (ACS) distributions.

5.1. Small-angle x-ray scattering (SAXS)

5.1.1. Log-normal fit

Figure 4 shows the measured SAXS intensity $I(q)$. The data was fitted with equation (7) using either the scattering length density contrast between particle and water $\Delta\rho_s = 31.1 \times 10^{-4}$ nm^{-2} for magnetite or $\Delta\rho_s = 28.6 \times 10^{-4}$ nm^{-2} for maghemite (table 1). A least squares fit resulted in $\phi_p^{Fe_3O_4} = 1.02(8) \times 10^{-3}$ and $\phi_p^{\gamma-Fe_2O_3} = 1.2(1) \times 10^{-3}$, respectively. These values for ϕ_p are in good agreement with the particle

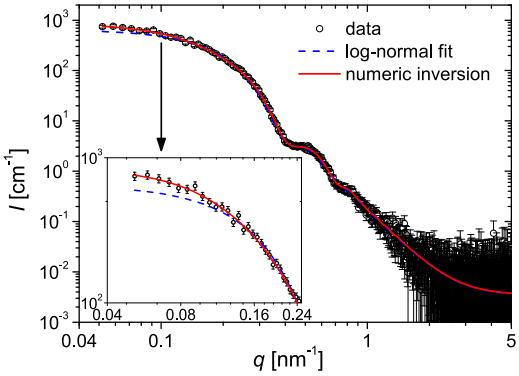

Figure 4. SAXS scattering intensity $I(q)$ of the colloidal dispersion, fitted with equation (7) (dashed line) and reconstructed data with $c_S \cdot p_N^{sum}(d_c)$ (figure 6), determined by numerical inversion (solid line). Inset shows the low q-range.

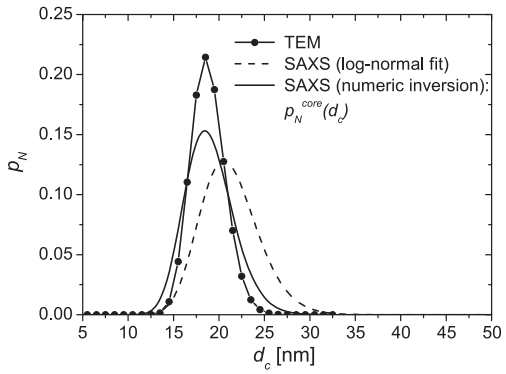

Figure 5. Number-weighted log-normal distribution of the core diameter d_c determined by TEM (figure 2) and by fitting the SAXS data (dashed line, figure 4). Solid line: number-weighted log-normal distribution $p_N^{core}(d_c)$ of the simulated core–shell particles from figure 7.

concentrations determined by ICP-OES (table 2). The obtained value for the background was $bkg = 3.4(2) \times 10^{-3}$ cm^{-1} and the determined log-normal distribution $p_N^{SAXS}(d_c)$ is shown in figure 5. The broadness of $p_N^{SAXS}(d_c)$ is $\sigma = 0.15(4)$ and the median $\bar{d}_{c,N} = 21(1)$ nm. Comparison with the distribution determined by TEM (figure 5, table 2) shows that the log-normal distribution according to SAXS is broader and shifted to larger values. It can be observed that in the low q-range of figure 4 the forward scattering of the sample is significantly enhanced compared to the fit, which indicates the presence of larger structures, i.e. agglomerates. To verify this we determined the discrete core-size distribution numerically.

5.1.2. Numerical inversion

We numerically inversed the data using the form factor of a sphere as model function (equation (14)) to extract the particle size distribution $p_N(d_c)$. In doing so, the incoherent scattering background bkg can be, in principal, implemented as a fitting parameter [35], however, here the result $bkg = 3.4 \times 10^{-3}$ cm^{-1} from the log-normal fit was used. For the inversion the range of the histogram $p_N(d_c)$ was set to be from $d_c = 1$–50 nm in $\Delta d_c = 0.5$ nm steps ($N = 99$).

Figure 6 shows, for the 200 α values, the determined distributions $c_S \cdot p_N^{\alpha}(d_c)$ and the inset of figure 6 the corresponding probabilities $P(\alpha)$. The average distribution $c_S \cdot p_N^{sum}(d_c)$ was calculated using equation (A.9). Reconstruction of $I(q)$ with equation (A.6) for $P(z_j) = c_S \cdot p_N^{sum}(d_{c,j})\Delta d_{c,j}$ resulted in very good agreement with the experimental data over the whole q-range (figure 4).

The prefactor $c_S = \phi_p \Delta\rho_s^2 / \langle V_c \rangle$ (equation (14)) can be determined to be $c_S = c_S \sum_{j=1}^{N} p_N^{sum}(d_{c,j})\Delta d_{c,j} = 2.04 \times 10^{37}$ cm^{-7} and the mean volume to be $\langle V_{c,N} \rangle = \sum_{j=1}^{N} p_N^{sum}(d_{c,j}) V_c(d_{c,j}) \Delta d_{c,j} = 5011$ nm^3. Using the same values for the scattering length density contrast as above ($\Delta\rho_s^{Fe_3O_4} = 31.1 \times 10^{-4}$ nm^{-2}, $\Delta\rho_s^{\gamma-Fe_2O_3} = 28.6 \times 10^{-4}$ nm^{-2}) the calculated volume concentrations were $\phi_p^{Fe_3O_4} = 1.05 \times 10^{-3}$ and $\phi_p^{\gamma-Fe_2O_3} = 1.25 \times 10^{-3}$, which matches well with the log-normal fit and ICP-OES (table 2).

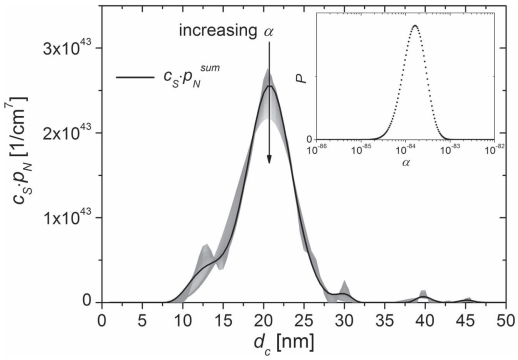

Figure 6. Gray lines: 200 discrete core-size distributions $c_S \cdot p_N^{\alpha}(d_c)$ determined by numerical inversion of $I(q)$ (figure 4). Inset: corresponding evidence values $P(\alpha)$. Black line: weighted average $c_S \cdot p_N^{sum}(d_c)$.

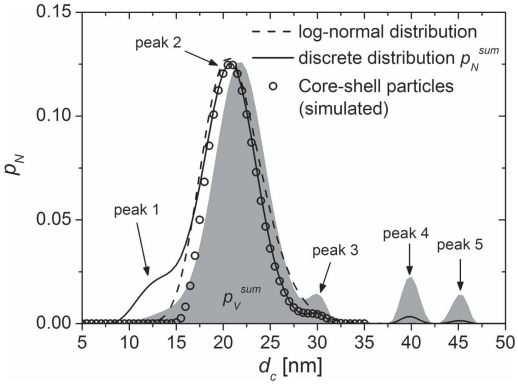

Figure 7. The number-weighted log-normal distribution of the core diameter d_c determined by fitting the SAXS data under the assumption of a log-normal distribution (dashed line, figure 5). The discrete distribution $p_N^{sum}(d_c)$ determined by numerical inversion (full line, figure 6). Circles: distribution determined for simulated core–shell particles with a 2 nm thick shell and the core diameter distribution $p_N^{core}(d_c)$ displayed in figure 5. Gray area: volume-weighted distribution $p_V^{sum}(d_c) \propto p_N^{sum}(d_c) \cdot d_c^3$.

The comparison between the probability density $p_N^{sum}(d_c)$ and the log-normal distribution $p_N^{SAXS}(d_c)$ (figure 7) shows that the main peak (peak 2) is at the same position as $p_N^{SAXS}(d_c)$, but that $p_N^{SAXS}(d_c)$ is slightly broader. Also, by numerical inversion some additional features are observed (peak 1, peak 3, peak 4, peak 5). The shoulder of $p_N^{sum}(d_c)$ at small d_c (peak 1) indicates the presence of a fraction of smaller particles not observed in TEM. Peak 3 on the other hand can be attributed to a few nm thick polymer layer on the particles (figure 1). This means that the extracted distribution $p_N^{sum}(d_c)$ does not represent the real core-size distribution of the IONPs. The reason for this is that the data was inversed using the form factor of a homogeneous sphere, neglecting the surrounding polymer (DMSA) layer. To verify this, peaks 2 and 3 of the determined distribution $p_N^{sum}(d_c)$ were further analyzed with the goal of extracting the real core-size distribution of the individual particles.

To get a deeper physical understanding of the results, we investigated what a core–shell model [50] predicts regarding the extracted size distribution. For this purpose we simulated the scattering intensity $I^{sim}(q)$ of an ensemble of IONPs surrounded by a surfactant layer with the core–shell model [50], assuming a log-normal distribution of the core sizes. The free parameters in the core–shell model were (i) the shell (surfactant) thickness s (figure 1), (ii) the scattering length density ρ_s^{shell} of the shell and (iii) the broadness σ and median value $\bar{d}_{c,N}$ of the number-weighted core-size distribution. Afterwards, $I^{sim}(q)$ was numerically inversed the same way as the experimental data and the free parameters adjusted until good agreement between the extracted distribution and peaks 2 and 3 of $p_N^{sum}(d_c)$ was obtained (figure 7). This approach is comparable to a core–shell model fit of the reciprocal scattering data $I(q)$, which is the standard approach to analyzing the structural properties of nanoparticles surrounded by a surfactant layer [56]. The difference, however, is that we can analyze separately the scattering behavior of the individual particles, which is achieved by focusing on the adjustment of peaks 2 and 3. By contrast, a fit of $I(q)$ would include all scattering contributions (peaks 1–5).

The best agreement between $p_N^{sum}(d_c)$ and the distribution of the simulated ensemble shown in figure 7 was found for: (i) a thickness of $s = 2$ nm of the surfactant layer (figure 1), (ii) a scattering length density of the

Table 3. Main results of the SAXS, DCM and ACS data analysis of the colloidal dispersion by numerical inversion. SAXS: number-weighted log-normal distribution $p_N^{core}(d_c)$ of core size d_c with broadness σ, median value $\bar{d}_{c,N}$ and mean value $\langle d_{c,N}\rangle$ as well as the volume fraction of individual particles ϕ_{ip}^{SAXS}. DCM: volume-weighted mean moment $\langle \mu_{ip,V}\rangle$, number-weighted mean magnetic core diameter $\langle d_{m,N}\rangle$ and volume fraction of individual particles ϕ_{ip}^{DCM}. ACS: number-weighted log-normal distribution of hydrodynamic diameter d_h with broadness σ, median value $\bar{d}_{h,N}$ and mean value $\langle d_{h,N}\rangle$ as well as effective anisotropy constant K.

SAXS (colloid)		DCM (colloid)		ACS (colloid)	
σ	0.14	$\langle \mu_{ip,V}\rangle$	1.91×10^{-18} A m^2	σ	0.38
$\bar{d}_{c,N}$	18.8 nm	$\langle d_{m,N}\rangle$	18.0 nm	$\bar{d}_{h,N}$	30 nm
$\langle d_{c,N}\rangle$	19.0 nm	ϕ_{ip}^{DCM}	0.92	$\langle d_{h,N}\rangle$	32.2 nm
ϕ_{ip}^{SAXS}	0.92			K	9 kJ m^{-3}

surfactant ρ_s^{shell} with $\rho_s^{shell} = 0.38 \cdot \rho_s^{core}$ and (iii) a log-normal core-size distribution with $\sigma = 0.14$, $\bar{d}_{c,N} = 18.8$ nm and hence $\langle d_{c,N}\rangle = 19.0$ nm. This distribution $p_N^{core}(d_c)$ is plotted in figure 5 and, as can be seen, is in accordance with the core-size distribution determined by TEM (table 2), just slightly broader. In the following we will regard the distribution $p_N^{core}(d_c)$ as the real core-size distribution of the individual IONPs according to SAXS.

Furthermore, numerical inversion offers the opportunity of observing and hence characterizing larger structures present in the dispersion by analyzing the peaks in the large d_c-range (peaks 4 and 5 in figure 7). We surmise that these larger structures are particle agglomerates. With sizes in the range 37–47 nm the agglomerates apparently consist of only a few particles (~2–8).

The number of agglomerates appears to be insignificant compared to the number of individual particles. But transforming the number-weighted distribution $p_N^{sum}(d_c)$ to a volume-weighted distribution $p_V^{sum}(d_c) \propto p_N^{sum}(d_c) \cdot d_c^3$ (figure 7, gray area) shows that a significant volume fraction of the particles seems to be agglomerated. This volume fraction ϕ_{agg} can be estimated by integrating over the peaks at 40 and 45 nm in figure 7 (peaks 4 and 5) to $\phi_{agg} \approx 0.08$. Consequently, the volume fraction of individually dispersed particles amounts to $\phi_{ip}^{SAXS} = 0.92$ according to SAXS.

In summary, via the analysis of the discrete size distribution $p_N^{sum}(d_c)$ we estimated the real core-size distribution of the individual particles (not agglomerated) to be the log-normal distribution $p_N^{core}(d_c)$, with $\sigma = 0.14$, $\bar{d}_{c,N} = 18.8$ nm and thus $\langle d_{c,N}\rangle = 19.0$ nm. Additionally, we evaluated the volume fraction of individual particles to be about $\phi_{ip}^{SAXS} = 0.92$. The central results are summarized in table 3 and compared in the following with the results obtained from the analysis of the DCM and ACS data.

5.2. Isothermal magnetization (DCM)

5.2.1. Log-normal fit

In figure 8 the complete isothermal magnetization measurement in the field range $\mu_0 H = \pm 4.9$ T is shown. The magnetization at $\mu_0 H = 4.9$ T is 126.1 A m^2 kg$_{Fe}^{-1}$, which is close to the saturation magnetization of bulk magnetite $M_S^{Fe_3O_4} = 128.3$ A m^2 kg$_{Fe}^{-1}$ (table 1). That the magnetization curve is not completely saturated, even at 4.9 T, can be attributed to a paramagnetic-like contribution of uncorrelated surface spins [39, 57]. To correct the magnetization curve from all linear contributions in the high field range, the last three data points were fitted linearly to obtain χ_p (A m^2 kg$_{Fe}^{-1}$ T^{-1}) and $\chi_p \mu_0 H$ is subtracted. We used the corrected data set for the log-normal fit and the numerical inversion.

We obtained the best fit result of the initial magnetization branch ($\mu_0 H = 0 \rightarrow 4.9$ T) using equation (10) for a log-normal distribution of the magnetic core sizes with $\sigma = 0.37(2)$, $\bar{d}_{m,N} = 12.2(5)$ nm and hence $\langle d_{m,N}\rangle = 13.1(5)$ nm. The comparison of the extracted magnetic core-size distribution with the core-size distributions determined by TEM (table 2) or SAXS (table 3) shows significant differences. Additionally, large, systematic deviations between the experimental data and the fit are observed (figures 8 and 9). Two possible contributing factors to the deviations are (i) the unknown magnetization behavior of the surface spins and (ii) particle agglomerates. From these discrepancies it can be concluded that the isothermal magnetization behavior of the colloidal particle ensemble cannot be modeled *ad hoc* by a single log-normal distribution, which has also been observed for other systems [57, 58]. To verify this, we determined the apparent moment distribution of the particles by numerical inversion.

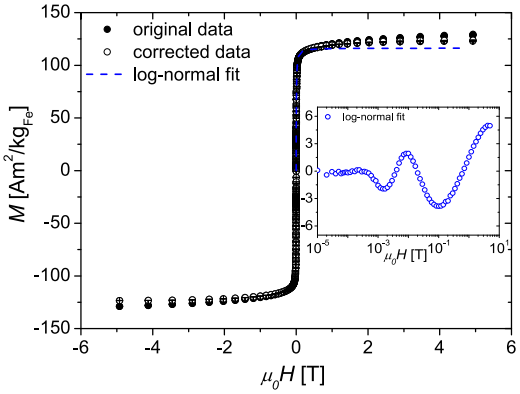

Figure 8. Isothermal magnetization curve of the colloidal dispersion and data corrected from linear contributions in the high field range. Dashed line: fit of corrected data under the assumption of a log-normal distribution of the magnetic core diameter d_m (equation (10)). Inset: residuals of the log-normal fit.

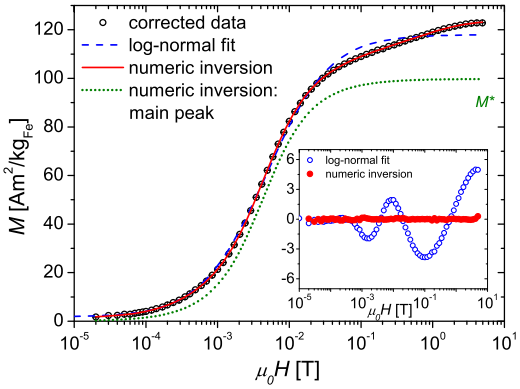

Figure 9. Isothermal magnetization curve and fit from figure 8 in logarithmic field scale. Solid line: $M(H)$ reconstructed with $c_D \cdot p_V^{sum}(\mu)\Delta\mu$ (figure 10). Dotted line: $M^*(H)$ reconstructed using only the main peak of $c_D \cdot p_V^{sum}(\mu)\Delta\mu$. Inset: residuals of the log-normal fit and numerical inversion.

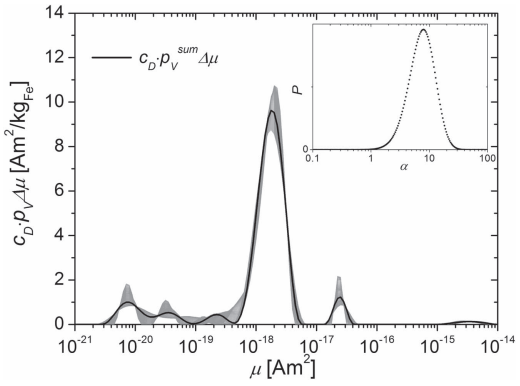

Figure 10. Gray lines: 200 discrete moment distributions $c_D \cdot p_V^{\alpha}(\mu)\Delta\mu$ determined by numerical inversion of $M(H)$ (figure 9). Inset: corresponding evidence values $P(\alpha)$. Black line: weighted average $c_D \cdot p_V^{sum}(\mu)\Delta\mu$.

5.2.2. Numerical inversion

We inversed the data with equation (15) to extract $p_V(\mu)$. The range of the extracted moment distribution was set to be 10^{-21}–10^{-14} Am^2, divided into $N = 141$ bins (20 points per decade) with a logarithmic spacing $\Delta\mu_j$. Figure 10 shows the 200 determined distributions $c_D \cdot p_V^{\alpha}(\mu)\Delta\mu$, the corresponding probabilities $P(\alpha)$ and the mean distribution $c_D \cdot p_V^{sum}(\mu)\Delta\mu$. Reconstruction of $M(H)$ with $P(\mu) = c_D \cdot p_V^{sum}(\mu)\Delta\mu$ results in very good

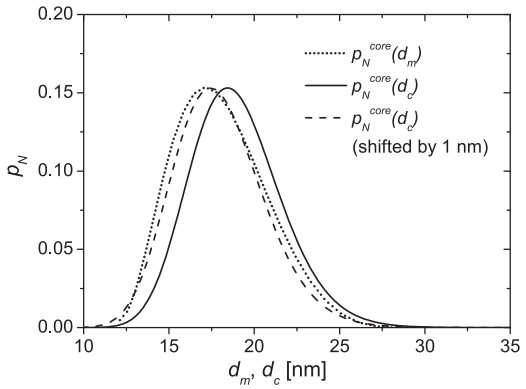

Figure 11. Number-weighted magnetic core diameter distribution $p_{\mathrm{N}}^{\mathrm{core}}(d_{\mathrm{m}})$ (dotted line) determined by transforming the main peak of the moment distribution $c_{\mathrm{D}} \cdot p_{\mathrm{V}}^{\mathrm{sum}}(\mu)\Delta\mu$ (figure 10) and the number-weighted core diameter distribution $p_{\mathrm{N}}^{\mathrm{core}}(d_{\mathrm{c}})$ from figure 5 (solid line). Dashed line: $p_{\mathrm{N}}^{\mathrm{core}}(d_{\mathrm{c}})$ shifted by 1 nm.

agreement with the experimental data (figure 9). As shown in figure 9, the residuals are nearly zero over the whole field range, indicating the high quality of the fit by numerical inversion. Therefore, the extracted moment distribution $c_{\mathrm{D}} \cdot p_{\mathrm{V}}^{\mathrm{sum}}(\mu)\Delta\mu$ seems to be a very good representation of the real intrinsic moment distribution.

Over the whole μ-range several peaks in $c_{\mathrm{D}} \cdot p_{\mathrm{V}}^{\mathrm{sum}}(\mu)\Delta\mu$ can be observed. In the following we assume that the main peak at $\sim 10^{-18}$ Am^2 corresponds to the magnetic cores of the individually dispersed nanoparticles, whose magnetization behavior can be modeled over the whole field range, each by a single Langevin function. The other peaks describe magnetization contributions that lead to deviations from the simple Langevin-type behavior, e.g. the uncorrelated surface spins or agglomerates [59, 60].

The main peak in figure 10 starts at the index $j = 54$ and ends at $j = 78$. The volume-weighted mean moment of the individual cores is determined from the main peak to $\langle \mu_{\mathrm{ip,V}} \rangle = 1.91 \times 10^{-18}$ Am^2. The reconstruction of the magnetization curve with only the contributions of the main peak results in the curve $M^*(H) = c_{\mathrm{D}} \sum_{j=54}^{78} p_{\mathrm{V}}^{\mathrm{sum}}(\mu_j) L(H_i, \mu_j) \Delta\mu_j$, also shown in figure 9. At 4.9 T this curve reaches a value of $M^*(4.9\ \mathrm{T}) = 99.8\ \mathrm{Am^2\ kg_{Fe}^{-1}}$ and is basically completely saturated. With this information the contribution of the magnetic cores of the individual particles to the total magnetization of the sample can be estimated to be $\phi_{\mathrm{imc}} = M^*(4.9\ \mathrm{T})/M_{\mathrm{S}}^{\mathrm{Fe_3O_4}} = 0.78$. Assuming a homogeneous magnetization, this means that the magnetic cores of the individual particles (non-agglomerated/non-interacting) constitute a volume fraction of $\phi_{\mathrm{imc}} = 0.78$ of the total sample (iron oxide). This is below the volume fraction $\phi_{\mathrm{ip}}^{\mathrm{SAXS}} = 0.92$ of individually dispersed particles according to SAXS (table 3). The discrepancy between $\phi_{\mathrm{imc}} = 0.78$ and $\phi_{\mathrm{ip}}^{\mathrm{SAXS}} = 0.92$ can be attributed to the reduced magnetic core volume compared to the total particle core volume due to the surface layer with uncorrelated spins. This can be shown by transforming the main peak of the extracted moment distribution to a number-weighted magnetic core-size distribution $p_{\mathrm{N}}^{\mathrm{core}}(d_{\mathrm{m}})$.

To determine $p_{\mathrm{N}}^{\mathrm{core}}(d_{\mathrm{m}})$ we transformed the main peak of the discrete moment distribution as follows. First the moments μ_j were converted to $d_{\mathrm{m},j} = (6\mu_j/(\pi M_{\mathrm{S}}))^{1/3}$ with $M_{\mathrm{S}} = 0.48$ MA m^{-1} (table 1) and the discrete values $c_{\mathrm{D}} p_{\mathrm{V}}^{\mathrm{sum}}(\mu_j)\Delta\mu_j = c_{\mathrm{D}} p_{\mathrm{V}}^{\mathrm{sum}}(d_{\mathrm{m},j})\Delta d_{\mathrm{m},j}$ were divided by $c_{\mathrm{D}} = M_{\mathrm{S}} = 128.3$ A m^2 kg$_{\mathrm{Fe}}^{-1}$. In the next step the values $p_{\mathrm{V}}^{\mathrm{sum}}(d_{\mathrm{m},j})\Delta d_{\mathrm{m}_j}$ were divided by the corresponding volume $V_{\mathrm{m},j}$ and by the weight $\Delta d_{\mathrm{m},j}$. Finally, the histogram was normalized so that $\int_0^\infty p_{\mathrm{N}}^{\mathrm{core}}(d_{\mathrm{m}})\mathrm{d}d_{\mathrm{m}} = 1$. In figure 11 the resulting distribution $p_{\mathrm{N}}^{\mathrm{core}}(d_{\mathrm{m}})$ is plotted.

Compared to the core-size distribution $p_{\mathrm{N}}^{\mathrm{core}}(d_{\mathrm{c}})$ determined by SAXS (table 3), the magnetic core-size distribution is shifted to lower values. The number-weighted mean value of the magnetic core size is $\langle d_{\mathrm{m,N}} \rangle = \sum_{j=1}^{N} p_{\mathrm{N}}^{\mathrm{core}}(d_{\mathrm{m},j}) d_{\mathrm{m},j} \Delta d_{\mathrm{m},j} = 18.0$ nm. This is 1 nm below the mean value of the core size according to SAXS ($\langle d_{\mathrm{c,N}} \rangle = 19.0$ nm). As illustrated in figure 1, this indicates (on average) a shell thickness of uncorrelated surface spins of 0.5 nm. Accordingly, very good agreement between the core size and magnetic core-size distribution is found when $p_{\mathrm{N}}^{\mathrm{core}}(d_{\mathrm{c}})$ is shifted by 1 nm ($d_{\mathrm{m}} = d_{\mathrm{c}} - 1$ nm).

With this information the volume fraction ϕ_{mc} of the total particle volume, which is homogeneously magnetized, can be estimated to be on average $\phi_{\mathrm{mc}} = \langle d_{\mathrm{m,N}} \rangle^3 / \langle d_{\mathrm{c,N}} \rangle^3 = 0.85$. Hence, according to the DCM measurement the volume fraction of individual particles within the ensemble is $\phi_{\mathrm{ip}}^{\mathrm{DCM}} = \phi_{\mathrm{imc}} / \phi_{\mathrm{mc}} = 0.78/0.85 = 0.92$. This is in very good agreement with the results from SAXS, where the volume fraction of the individual particles was also determined to be $\phi_{\mathrm{ip}}^{\mathrm{SAXS}} = 0.92$ (table 3). Accordingly, the volume fraction of agglomerated particles can be estimated to be $\phi_{\mathrm{agg}}^{\mathrm{DCM}} = 0.08$.

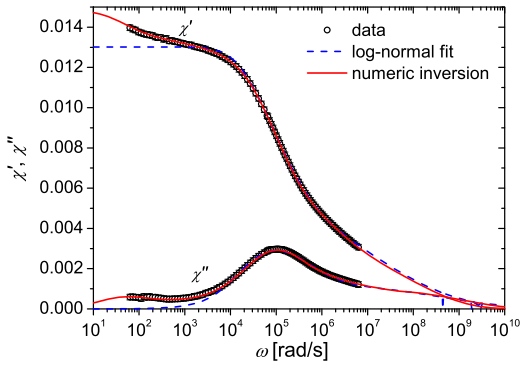

Figure 12. Real and imaginary part of the complex volume susceptibility of the colloidal dispersion measured by ACS. Dashed lines: fit of $\chi'(\omega)$ and $\chi''(\omega)$ with equation (11) under the assumption of a bimodal distribution $p(\tau)$ (superposition of two log-normal distribution). Solid line: reconstructed data set for the discrete relaxation time distribution $c_A \cdot p^{sum}(\tau)\Delta\tau$ determined by numerical inversion (figure 13).

With the DCM measurement of the immobilized particles the volume fraction of thermally blocked particles was determined to be $\phi_{TB} = 0.12$ (table 2). The quite good agreement between ϕ_{agg}^{DCM} and ϕ_{TB} could indicate that most of the agglomerated particles are thermally blocked, due to dipolar interactions. As shown in [60], a blocking of the macrospins in agglomerates of normally superparamagnetic particles can result in increased effective moments of the agglomerates, compared to the individual particles. This could also explain the observed peak in the high moment range (10^{-17}–10^{-18} Am^2) in the extracted moment distribution (figure 10). Accordingly, the agglomerates can significantly contribute to the ACS spectra of the colloidal dispersion, as shown in the following.

The peaks in the low moment range on the other hand correlate to non-linear magnetization processes in the high field range. We surmise that they can be either attributed to dipolar interactions within the agglomerates [59] or to uncorrelated surface spins.

5.3. Frequency dependent AC susceptibility (ACS)

5.3.1. Log-normal fit

Figure 12 shows the real and imaginary part of the measured volume susceptibility $\tilde{\chi}(\omega)$. In the imaginary part a pronounced peak at $\sim 10^5$ rad/s is observed, which correlates to a characteristic relaxation time of $\tau = 10^{-5}$ s. In the case of Brownian relaxation (equation (4), $\eta = 1$ mPa s^{-1} for water), a relaxation time of $\tau_B = 10^{-5}$ s corresponds to a hydrodynamic size of $d_H \approx 30$ nm, which is below the z-average measured by DLS ($\langle d_{h,I} \rangle = 52$ nm, table 2). But with DLS we determined the intensity-weighted mean of the hydrodynamic diameter, and the expected volume- or number-weighted means would, in theory, be significantly smaller. Thus we surmise that the peak at $\sim 10^5$ rad/s is mostly a result of Brownian relaxation processes.

To fit measurements of polydisperse nanoparticle ensembles, however, normally Néel contributions also have to be considered, which is done for example in the generalized Debye model [14, 51, 52]. Qualitatively, this model is comparable to the superposition of two log-normal functions $p(\tau) = a \cdot p_1(\tau) + (1 - a) \cdot p_2(\tau)$ in equation (11) in the case that Néel and Brownian contributions do not overlap. Fitting χ' and χ'' under the assumption of a bimodal distribution of relaxation times resulted in the high frequency part ($\omega > 10^4$ Hz) in good agreement with the data (figure 12). From the extracted relaxation time distributions structural parameters such as the hydrodynamic size or the magnetic core size can be determined [14, 51, 52]. However, as can be seen in figure 12, in the low frequency range significant deviations between data and fit are observed, which indicates the presence of slow relaxation processes. It is safe to assume that these can be attributed to the contributions from particle agglomerates. To extract the complete spectra of relaxation times we numerically inversed the experimental data using equation (16) as a model function.

5.3.2. Numerical inversion

To adjust the experimental data shown in figure 12 over the whole ω range, the range of the extracted relaxation time distribution had to be set to $10^{-10} - 10^0$ s. The histogram was divided into $N = 181$ bins (20 points per decade) with a logarithmic spacing $\Delta\tau_j$. Figure 13 shows the 200 determined distributions $c_A \cdot p^{\alpha}(\tau)\Delta\tau$, the corresponding probabilities $P(\alpha)$ and the average distribution $c_A \cdot p^{sum}(\tau)\Delta\tau$. Due to the missing information in the very high and low frequency range (no data points in the ACS spectra) the solutions for the extracted relaxation time distribution in the very low and high time range are not reliable [61, 62]. The time ranges with

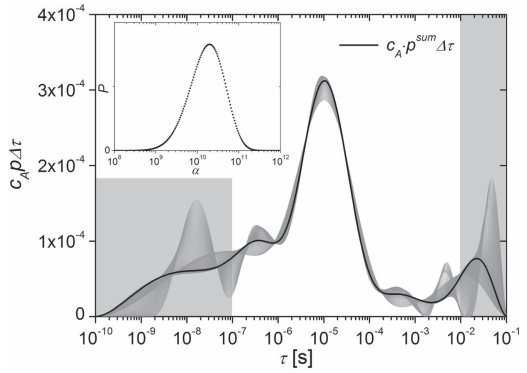

Figure 13. Gray lines: 200 discrete relaxation time distributions $c_A \cdot p^{\alpha}(\tau)\Delta\tau$ determined by the simultaneous numerical inversion of $\chi'(\omega)$ and $\chi''(\omega)$ (figure 12). Ranges of unreliable solutions are indicated by gray areas. Inset: corresponding evidence values $P(\alpha)$. Solid line: weighted average $c_A \cdot p^{sum}(\tau)\Delta\tau$.

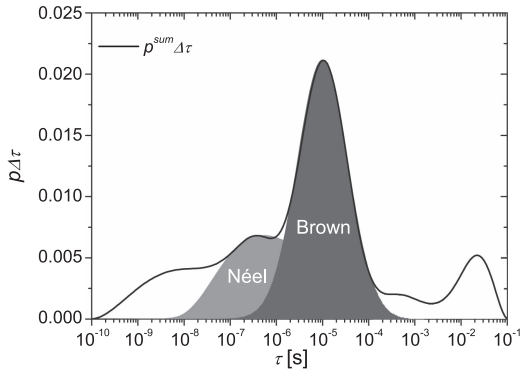

Figure 14. Solid line: average relaxation time distribution $p^{sum}(\tau)\Delta\tau$ from figure 13. Dark gray area: distribution of Brownian relaxation times $P(\tau_b)\Delta\tau_b$ calculated with equation (4) for a number-weighted log-normal distribution of the hydrodynamic diameter d_h with $\sigma = 0.42$ and $\bar{d}_{h,N} = 35.5$ nm. Light gray area: Néel relaxation times $P(\tau_n)\Delta\tau_n$ calculated with equation (3) for the magnetic core diameter distribution $p_N^{sum}(d_m)$ from figure 11 (red line). The points of both distributions $P(\tau_b)\Delta\tau_b$ and $P(\tau_n)\Delta\tau_n$ are logarithmically spaced and weighted accordingly.

unreliable information can be roughly estimated to be $\tau < 10^{-7}$ s and $\tau > 10^{-2}$ s, as indicated in figure 13 by the gray areas.

In the region $\tau = 10^{-7}$–10^{-2} s with reliable solutions, two peaks can be identified. The main peak at $\sim 10^{-5}$ s and a smaller peak (shoulder) at $\sim 3 \times 10^{-7}$ s. As mentioned before, the main peak seems to correspond to the Brownian relaxation of the individually dispersed and thermally blocked particles, whereas the smaller peak can be attributed to small particles, which respond by Néel relaxation. The remaining very small relaxation times can be probably attributed to intra-well relaxation processes [63, 64] (transversal relaxation). Additionally, contributions in the very large relaxation time range are observed (10^{-3}–10^{-1} s). As mentioned before, it is safe to assume that these slow processes correspond to the relaxation dynamics of the agglomerated particles, as discussed for example in [14].

Hence, by numeric inversion we could isolate the different contributions and subsequently analyze them separately. First, we estimated the hydrodynamic diameter distribution of the particles from the main peak of $p^{sum}(\tau)\Delta\tau$. Considering that now the individually dispersed particles could be analyzed separately, we could assume a log-normal shape for the hydrodynamic size distribution.

For this purpose, we calculated the Brownian relaxation time distribution $P(\tau_b)$ with equation (4) for a given log-normal distribution of the hydrodynamic diameter d_h until visually good agreement was found between $P(\tau_b)\Delta\tau_b$ and the main peak. The distribution $P(\tau_b)\Delta\tau_b$ shown in figure 14 was obtained for a number-weighted log-normal distribution of d_h with $\sigma = 0.38$, $\bar{d}_{h,N} = 30$ nm and thus $\langle d_{h,N}\rangle = 32$ nm. As already mentioned at the beginning of this section, this is significantly below the z-average measured by DLS ($\langle d_{h,I}\rangle = 52$ nm, table 2), which can be mainly attributed to the fact that by DLS the intensity-weighted mean is determined.

To analyze if the second peak at $\sim 3 \times 10^{-7}$ s could be in fact attributed to Néel relaxation, we calculated the expected distribution $P(\tau_n)\Delta\tau_n$ with equation (3) using the magnetic core diameter distribution determined by

DCM (figure 11). The distribution $P(\tau_n)\Delta\tau_n$ shown in figure 14 was obtained when the anisotropy constant was set to $K = 9$ kJ m^{-3}, which is inbetween the magnetocrystalline anisotropy constant of bulk magnetite and maghemite (table 1). The quite good agreement with $p^{sum}(\tau)\Delta\tau$ seems to verify that this peak corresponds to the Néel relaxation of small particles. With $K = 9$ kJ m^{-3} the estimated effective anisotropy constant is in good agreement with other studies, where K was derived from ACS measurements and found to be in the range of $K = 10$ kJ m^{-3} for similar iron oxide nanoparticles [14, 65]. However, it has to be taken into account that in the case of cubic anisotropy the expected value for the effective anisotropy constant relevant for equation (3) would be $(1/12)|K_1|$ [66] and hence much lower than $K = 9$ kJ m^{-3}. A possible explanation for this discrepancy is that the effective anisotropy constant of the IONPs is dominated by surface anisotropy, as theorized in [67].

6. Final remarks

Prior to an application of magnetic nanoparticles, for example in biomedicine, the main physical properties of the ensembles (structural as well as magnetic) must be evaluated, ideally in a standardized way [5, 6]. Amongst other properties, of outmost importance is knowledge on the characteristic particle sizes, such as core, magnetic and hydrodynamic size. The usual approach to determining the relevant size distributions from measurements (scattering, magnetization, susceptibility) is to assume *a priori* a log-normal shape and fit the data accordingly [10–14]. However, subtle details relevant for the application of magnetic nanoparticles can be missed, as we have revealed in our results described above. Our numerical inversion procedure, derived from a method used for the analysis of small-angle scattering data [34, 35], is a finer approach to revealing the distribution functions. This method does not imply a complication in deriving the relevant physical parameters compared to classical model fits but in fact our aim is to reach an easily applicable numerical approach. For this purpose the applied model functions are intended to be kept as simple as possible.

In this study we initially extracted the particle size distribution of an ensemble of iron oxide nanoparticles by numerical inversion from SAXS data of the colloidal particle dispersion. Then we determined the moment distribution of the particle ensemble from the isothermal magnetization (DCM) measurement and its relaxation time distribution from the ACS measurement of the colloidal dispersion, using the same numerical approach. As model functions we simply used the particle form factor of a sphere (SAXS), the Langevin function (DCM) and the Debye model (ACS). In figures 6, 10 and 13 the extracted size, moment and relaxation time distributions are shown. In all three cases the distributions deviate from the commonly expected log-normal shape.

These deviations are well interpreted as stemming partly from particle agglomerates (SAXS, DCM, ACS). It also appears, unambiguously, that uncorrelated surface spins modify the expected magnetization behavior (DCM). Such surface spins are a common finding in magnetic nanoparticles as described, e.g., in [39–44]. Finally, a good description of the relaxation time spectra may be connected to the presence of intra-well relaxation processes [63, 64]. Accordingly, the distributions determined by numerical inversion exhibit characteristic peaks, which we attributed to these contributions. However, we additionally observed peaks in the discrete distributions, which we could distinctly ascribe to the individually dispersed and non-interacting particles. Ultimately, evaluation of these peaks allowed us to estimate their core, magnetic core and hydrodynamic sizes as well as relevant ensemble parameters, summarized in table. 3.

According to these results the mean core size of the particles was 19 nm and the mean magnetic core size 18 nm. This indicated the presence of a 0.5 nm thick surface layer of uncorrelated surface spins. Furthermore, from an analysis of the as determined size and moment distributions we calculated the volume fraction of agglomerated particles to be 0.08. From the extracted relaxation time distribution we estimated the hydrodynamic size distribution of the particles to have a mean value of 32.2 nm. Additionally, we could evaluate the effective anisotropy constant to be 9 kJ m^{-3}, which is in good agreement with other studies where K was derived from ACS measurements [14, 65].

Taking all these comments together it can be concluded that the analysis of the discrete distribution functions extracted by numerical inversion enables a detailed analysis of the structural and magnetic properties of the particle ensemble. This is fundamental for technical application and related standardization criteria. Naturally, the inversion method cannot eliminate the errors caused by an inadequacy of the applied model functions, which need to be carefully chosen. The main strength of the numerical inversion method is then the possible separation of contributions of the model-like contributions of the individually dispersed particles from the total measurement signal. The numerical approach to determining such distribution functions without *a priori* assumptions regarding the line shape is universally applicable, as we have shown in this study by means of scattering, magnetization and ACS data. The code for the numerical inversion of the SAXS, DCM and ACS data used for this study was written in Python and is available from the authors.

Acknowledgments

This project has received funding from the European Commission Framework Programme 7 under grant agreement no 604448.

Appendix: numerical inversion

Solving equation (13) is in general an ill-conditioned problem, in particular due to measurement uncertainties. This can give rise to large, unphysical oscillations in the extracted distribution. To overcome this problem two approaches were combined. First, a non-negative constraint [68] was implemented as done in [26, 28] to ensure positive values $P(z_j) > 0$ in the extracted distributions. Additionally, a Tikhonov regularization was applied to force smooth distributions. In this case, instead of equation (13) the functional [69]

$$\frac{1}{2\sigma^2} \|\mathbf{A}P(z) - D(x)\|^2 + \alpha \|\mathbf{L}P(z)\|^2 \tag{A.1}$$

is minimized, here additionally with the constraint $P(z) \geqslant 0$. The $N \times N$ matrix $\mathbf{L}$ is a regularization matrix which is generally chosen to force smooth solutions, weighted by the regularization parameter α. To additionally force the extracted distribution to approach zero at the start and end points the following non-singular approximation of the discrete second-order derivative operator was used:

$$\mathbf{L} = \frac{1}{2}\begin{pmatrix} 2 & 0 & & & \\ -1 & 2 & -1 & & \\ & \ddots & \ddots & \ddots & \\ & & -1 & 2 & -1 \\ & & & 0 & 2 \end{pmatrix}. \tag{A.2}$$

For numerical computation equation (A.1) is not suited and the least square solution of

$$\left\| \begin{bmatrix} \frac{1}{\sigma}\mathbf{A} \\ \sqrt{2\alpha}\mathbf{L} \end{bmatrix} P(z) - \begin{bmatrix} \frac{1}{\sigma}D(x) \\ 0_{N,1} \end{bmatrix} \right\|^2 \tag{A.3}$$

was determined for $P(z) \geqslant 0$, with $0_{N,1}$ being a zero vector of length N.

To find the optimal value for the regularization parameter α the *a posteriori* probability or evidence $P(\alpha)$ according to [35] was determined:

$$P(\alpha) \propto \frac{\exp(-\chi^2/2 - \alpha S)}{\det^{1/2}(\mathbf{H}/\alpha)}. \tag{A.4}$$

The χ^2 in equation (A.4) is defined in the usual manner, i.e.

$$\chi^2 = \sum_{i=1}^{M} \frac{(D_{\mathrm{rec}}(x_i) - D(x_i))^2}{\sigma(x_i)^2}, \tag{A.5}$$

with $D_{rec}(x_i)$ being the reconstructed data points:

$$D_{\mathrm{rec}}(x_i) = \sum_{j=1}^{N} A_{ij}P(z_j) = \sum_{j=1}^{N} A_{ij}c \cdot p(z_j)\Delta z_j. \tag{A.6}$$

In equation (A.4) the functional S is

$$S = \sum_{j=1}^{N} S_j \text{ with: } \vec{S} = (\mathbf{L} \cdot P(z))^2 \tag{A.7}$$

and $\mathbf{H}$ is the Hessian of the Tikhonov functional (equation (A.1)):

$$\mathbf{H} = \frac{1}{\sigma^2}\mathbf{A}^T\mathbf{A} + 2\alpha\mathbf{L}^2. \tag{A.8}$$

The approach was then as follows. First, the distribution $P(z)$ was determined for different α values—in the following labeled as $P^\alpha(z)$—by finding the least square solution of equation (A.3). Afterwards the *a posteriori* probability $P(\alpha)$ was calculated with equation (A.4) for the determined distribution $P^\alpha(z)$. This was done in all cases for 200 values of α, with α varying logarithmically spaced over several orders of magnitude. Finally the 200 distributions $P^\alpha(z)$ were summed up, weighted by the probability $P(\alpha)$ to calculate

$$P^{\mathrm{sum}}(z) = \frac{\sum_{i=1}^{200} P(\alpha_i) P^{\alpha_i}(z) \Delta\alpha_i}{\sum_{i=1}^{200} P(\alpha_i) \Delta\alpha_i}. \tag{A.9}$$

ORCID

P Bender https://orcid.org/0000-0002-2492-3956

References

[1] Pankhurst Q A, Connolly J, Jones S K and Dobson J 2003 *J. Phys. D: Appl. Phys.* **36** R167
[2] Gupta A K and Gupta M 2005 *Biomaterials* **26** 3995
[3] Laurent S, Forge D, Port M, Roch A, Robic C, Vander Elst L and Muller R N 2008 *Chem. Rev.* **108** 2064
[4] Wu W, Wu Z, Yu T, Jiang C and Kim W-S 2015 *Sci. Technol. Adv. Mater.* **16** 023501
[5] Posth O *et al* 2015 *in IMEKO XXI World Congress* **TC13** 1362–7 (http://www.imeko.org/publications/wc-2015/IMEKO-WC-2015-TC13-276.pdf)
[6] Mulvaney P, Parak W J, Caruso F and Weiss P S 2016 *ACS Nano* **10** 9763–4
[7] Coey J M D 2010 *Magnetism and Magnetic Materials* (Cambridge: Cambridge University Press)
[8] Skomski R 2008 *Simple Models of Magnetism* (Oxford: Oxford University Press on Demand)
[9] Skomski R 2003 *J. Phys.: Condens. Matter* **15** R841
[10] Chantrell R, Popplewell J and Charles S 1978 *IEEE Trans. Magn.* **14** 975
[11] El-Hilo M 2012 *J. Appl. Phys.* **112** 103915
[12] Luigjes B, Woudenberg S M, de Groot R, Meeldijk J D, Torres Galvis H M, de Jong K P, Philipse A P and Erné B H 2011 *J. Phys. Chem.* C **115** 14598
[13] Ludwig F, Guillaume A, Schilling M, Frickel N and Schmidt A M 2010 *J. Appl. Phys.* **108** 033918
[14] Ludwig F *et al* 2017 *J. Magn. Magn. Mater.* **427** 19
[15] Bean C P and Livingston J D 1959 *J. Appl. Phys.* **30** S120
[16] Debye P 1945 *Polar Molecules* (New York: Dover)
[17] Holm C, Ivanov A, Kantorovich S, Pyanzina E and Reznikov E 2006 *J. Phys.: Condens. Matter* **18** S2737
[18] Pyanzina E, Gudkova A, Donaldson J and Kantorovich S 2017 *J. Magn. Magn. Mater.* **431** 201
[19] Butter K, Bomans P, Frederik P, Vroege G and Philipse A 2003 *Nat. Mater.* **2** 88
[20] Klokkenburg M, Vonk C, Claesson E M, Meeldijk J D, Erné B H and Philipse A P 2004 *J. Am. Chem. Soc.* **126** 16706
[21] Allia P, Coisson M, Tiberto P, Vinai F, Knobel M, Novak M and Nunes W 2001 *Phys. Rev.* B **64** 144420
[22] Ivanov A O, Kantorovich S S, Reznikov E N, Holm C, Pshenichnikov A F, Lebedev A V, Chremos A and Camp P J 2007 *Phys. Rev.* E **75** 061405
[23] Pshenichnikov A, Lebedev A, Radionov A and Efremov D 2015 *Colloid J.* **77** 196
[24] Ivanov A O, Kantorovich S S, Zverev V S, Elfimova E A, Lebedev A V and Pshenichnikov A F 2016 *Phys. Chem. Chem. Phys.* **18** 18342
[25] Pshenichnikov A, Lebedev A, Lakhtina E and Kuznetsov A 2017 *J. Magn. Magn. Mater.* **432** 30
[26] Berkov D V, Görnert P, Buske N, Gansau C, Mueller J, Giersig M, Neumann W and Su D 2000 *J. Phys. D: Appl. Phys.* **33** 331
[27] Liu W, Zhou M and Kong L 2009 *Meas. Sci. Technol.* **20** 125802
[28] van Rijssel J, Kuipers B W and Erné B H 2014 *J. Magn. Magn. Mater.* **353** 110
[29] Schmidt D, Eberbeck D, Steinhoff U and Wiekhorst F 2017 *J. Magn. Magn. Mater.* **431** 33
[30] Pecora R 2000 *J. Nanoparticle Res.* **2** 123
[31] Zhu X, Shen J, Liu W, Sun X and Wang Y 2010 *Appl. Opt.* **49** 6591
[32] Glatter O 1977 *J. Appl. Crystallogr.* **10** 415
[33] Svergun D I and Koch M H J 2003 *Rep. Prog. Phys.* **66** 1735
[34] Hansen S 2000 *J. Appl. Crystallogr.* **33** 1415
[35] Vestergaard B and Hansen S 2006 *J. Appl. Crystallogr.* **39** 797
[36] Bender P *et al* 2017 *Sci. Rep.* **7** 45990
[37] Salas G, Casado C, Teran F J, Miranda R, Serna C J and Morales M P 2012 *J. Mater. Chem.* **22** 21065
[38] Roca A G, Veintemillas-Verdaguer S, Port M, Robic C, Serna C J and Morales M P 2009 *J. Phys. Chem.* B **113** 7033
[39] Morales M P, Veintemillas-Verdaguer S, Montero M I, Serna C J, Roig A, Casas L, Martinez B and Sandiumenge F 1999 *Chem. Mater.* **11** 3058
[40] Shendruk T N, Desautels R D, Southern B W and van Lierop J 2007 *Nanotechnology* **18** 455704
[41] Disch S, Wetterskog E, Hermann R P, Wiedenmann A, Vainio U, Salazar-Alvarez G, Bergström L and Brückel T 2012 *New J. Phys.* **14** 013025
[42] Dutta P, Pal S, Seehra M S, Shah N and Huffman G P 2009 *J. Appl. Phys.* **105** 07B501
[43] Echevarria-Bonet C *et al* 2013 *Phys. Rev.* B **87** 180407
[44] Iglesias O and Labarta A 2004 *Phys. B: Condens. Matter* **343** 286 proceedings of the Fourth Intional Conf. on Hysteresis and Micromagnetic Modeling
[45] Néel L 1955 *Adv. Phys.* **4** 191
[46] Günther A, Bender P, Tschöpe A and Birringer R 2011 *J. Phys.: Condens. Matter* **23** 325103
[47] Shliomis M 1974 *Phys.-Usp.* **17** 153
[48] Bogren S, Fornara A, Ludwig F, del Puerto Morales M, Steinhoff U, Hansen M F, Kazakova O and Johansson C 2015 *Int. J. Mol. Sci.* **16** 20308
[49] El-Hilo M and Chantrell R 2012 *J. Magn. Magn. Mater.* **324** 2593
[50] Pedersen J S 1997 *Adv. Colloid Interface Sci.* **70** 171
[51] Chung S-H, Hoffmann A, Guslienko K, Bader S, Liu C, Kay B, Makowski L and Chen L 2005 *J. Appl. Phys.* **97** 10R101
[52] Ludwig F 2010 *8th Int. Conf. Scientific and Clinical Applications of Magnetic Carriers* vol 1311 (Melville, NY: AIP Publishing) pp 249–54
[53] Chantrell R, Walmsley N, Gore J and Maylin M 2000 *Phys. Rev.* B **63** 024410

[54] Déjardin P-M 2011 *J. Appl. Phys.* **110** 113921
[55] Stoner E C and Wohlfarth E P 1991 *IEEE Trans. Magn.* **27** 3475
[56] Avdeev M V and Aksenov V L 2010 *Phys.-Usp.* **53** 971
[57] Eberbeck D, Dennis C L, Huls N F, Krycka K L, Gruttner C and Westphal F 2013 *IEEE Trans. Magn.* **49** 269
[58] Eberbeck D, Wiekhorst F, Wagner S and Trahms L 2011 *Appl. Phys. Lett.* **98** 182502
[59] Schaller V, Wahnström G, Sanz-Velasco A, Enoksson P and Johansson C 2009 *J. Magn. Magn. Mater.* **321** 1400
[60] Ahrentorp F *et al* 2015 *J. Magn. Magn. Mater.* **380** 221
[61] Davies A and Anderssen R 1997 *J. Non-Newton. Fluid Mech.* **73** 163
[62] Hansen S 2008 *Rheol. Acta* **47** 169
[63] Shliomis M and Stepanov V 1993 *J. Magn. Magn. Mater.* **122** 176
[64] Raikher Y L and Stepanov V I 1997 *Phys. Rev.* B **55** 15005
[65] Fannin P, Cohen-Tannoudji L, Bertrand E, Giannitsis A, Mac Oireachtaigh C and Bibette J 2006 *J. Magn. Magn. Mater.* **303** 147
[66] Aharoni A 1973 *Phys. Rev.* B **7** 1103
[67] Bødker F, Mørup S and Linderoth S 1994 *Phys. Rev. Lett.* **72** 282
[68] Lawson C L and Hanson R J 1995 *Solving Least Squares Problems* vol 15 (Philadelphia, PA: SIAM) doi:10.1137/1.9781611971217
[69] Tikhonov A N, Goncharsky A V, Stepanov V and Yagola A G 1995 *Numerical Methods for the Solution of Ill-Posed Problems* vol 328 (Dordrecht: Kluwer Academic)